ADVANCED THERAPEUTICS
www.advtherap.com

DNA-Based Nanocarriers to Sequester Altered microRNAs in Cardiac Dysfunction

Alejandro Postigo, Natalia Hernández-Bellido, Marcos Sánchez-Barat, Laura García-Mendívil, Esther Pueyo, Jesús del Barrio, Silvia Hernández-Ainsa, and Laura Ordovás**

MicroRNAs (miRs) play a critical role in modulating gene expression across biological processes, including cardiac aging and disease. As such, miRs have demonstrated therapeutic potential in several cardiac conditions. Efficient delivery of miR therapies to cardiac tissue is crucial for effective gene therapy and DNA-based nanocarriers (DNCs), based on Watson-Crick-Franklin highly specific base-pair recognition, have emerged as a promising, biocompatible alternative to viral-based methods. Here, DNCs designed to modulate miR levels as a potential treatment for cardiac dysfunction are presented. Specifically, the DNCs target miR-24-2, which inhibits *SERCA2* gene. In humans, the reduction of SERCA2 activity is a hallmark of heart failure and is altered in cardiac aging. The assembled DNCs bearing anti-miR-24-2-5p sequences effectively restore intracellular levels of SERCA2 in a HEK293 cell model. The DNCs proper assembly is thoroughly verified, while their stability and miR-capture ability are demonstrated in vitro. The DNCs exhibit successful internalization into HEK293 and modest uptake into human cardiomyocytes. SERCA2 restoration by DNCs is significantly influenced by the miR-capture sequence layout, underscoring the importance of precise design for optimal biological outcomes. This study highlights the potential of DNCs in cardiac therapies, a previously unexplored avenue for addressing cardiac dysfunction.

1. Introduction

Cardiovascular disease (CVD) currently stands as the foremost cause of global mortality and morbidity, accounting for ≈17.9 million deaths per year and constituting 32% of all-cause mortality.[1] Age is an independent risk factor for CVD, which is intricately linked to other pathological processes.[2] Therefore, the aging of the population, coupled with the prevalence of comorbidities, is expected to further consolidate and potentially exacerbate this epidemiological burden.[2,3] Moreover, the development of novel therapeutic approaches for the treatment of CVD is lagging behind, hampered by a lack of an in-depth understanding of the molecular pathways governing cardiac dysfunction.

miRs play a crucial role in regulating gene expression in many biological processes, including CVD and cardiac aging.[4–6] Due to their small size and pleiotropic effects, miRs are emerging as promising therapeutics. Consequently, the modulation of cardiac miRs has

A. Postigo†, J. del Barrio, S. Hernández-Ainsa
Instituto de Nanociencia y Materiales de Aragón (INMA)
CSIC-Universidad de Zaragoza
Zaragoza 50009, Spain
E-mail: silviamh83@unizar.es

N. Hernández-Bellido†, M. Sánchez-Barat, L. García-Mendívil, E. Pueyo, L. Ordovás
Instituto de Investigación en Ingeniería de Aragón (I3A)
Universidad de Zaragoza
Zaragoza 50018, Spain
E-mail: lordovas@unizar.es

The ORCID identification number(s) for the author(s) of this article can be found under https://doi.org/10.1002/adtp.202400247

†Equal contribution

DOI: 10.1002/adtp.202400247

N. Hernández-Bellido†, M. Sánchez-Barat, L. García-Mendívil, E. Pueyo, L. Ordovás
Instituto de Investigación Sanitaria (IIS) Aragón
Zaragoza 50009, Spain

E. Pueyo, L. Ordovás
Centro de Investigación Biomédica en Red de Bioingeniería Biomateriales y Nanomedicina (CIBER-BBN)
Zaragoza 50018, Spain

S. Hernández-Ainsa, L. Ordovás
Fundación ARAID
Gobierno de Aragón
Zaragoza 50018, Spain

demonstrated reparative and regenerative potential in the heart. For example, improved cardiac function in animal models of heart failure (HF) or myocardial infarction (MI)[7,8] has been reported and even a first-in-human trial in HF shows safety and cardiac functional improvements.[9]

miR-24-2 is upregulated in HF patients[10] and in aged human left ventricle (LV).[6] In addition, it is also implicated in the regulation of post-MI cardiac fibrosis.[11,12] miR-24-2-5p interacts with *SERCA2*,[6] a fundamental pump located in the sarcoplasmic reticulum of cardiomyocytes and whose activity is critical for controlling cardiac contractility and relaxation. Opposite to miR-24-2, *SERCA2* levels decrease with age and in HF.[6,13] Restoring SERCA2 levels currently represents a key pathway in gene therapy to address failing hearts[13] with several completed or ongoing *SERCA2* supplementation gene therapy trials (i.e., CUPID, MUSIC-HFrEF, or MUSIC-HFpEF). All of these trials are based on *SERCA2* delivery with Adeno-Associated Virus serotype 1 (AAV1), however, the existence of AAV1 neutralizing antibodies in humans[14] could compromise their success. Therefore, using non-viral methods to restore SERCA2 activity by inhibiting miR-24 in the cardiac tissue is a promising strategy for the treatment of cardiac dysfunction.

The direct administration of miR-regulatory therapies has exhibited only limited efficacy in human clinical trials for HF.[9] Likely limitations related to their nuclease sensitivity or rapid clearance limit effective dosing in the cardiac tissue. Additionally, systemic distribution of such approaches have been associated with adverse side effects in other pathologies.[15] In light of these limitations, nanocarriers are being avidly used to enhance the intracellular delivery of therapeutic nucleic acids, with the aim of improving the in vivo efficacy and safety of miR therapies.[16]

DNA-based nanocarriers (DNCs) have emerged as promising candidates for efficient delivery of miRs in vivo. Constructed using a bottom-up approach that relies on highly specific and programmable self-assembly of individual DNA oligonucleotides, DNCs have exhibited biocompatibility at the cellular level as well as in animal models,[14] with no systemic toxicity and low immunogenic response. [17] These favorable properties, combined with their straightforward and reproducible preparation, versatile design, functionality, and facile adaptability for targeted delivery, make DNCs suitable vehicles for therapeutic delivery in various applications, including chemotherapy,[18] gene therapy[19,20] or immunotherapy[21] among others. The chemical backbone of DNCs makes them particularly suited for gene delivery, as it can be tailored to harbor therapeutic sequences, such as antisense oligonucleotides (ASOs), messenger RNAs, miR mimics, antimiRs, and small interfering RNAs (siRNAs).[19]

In the context of miR-related therapy, DNA nanocages with truncated octahedral shapes,[22] RCA-based DNA nanosponges,[23] branched DNA nanostructures[24–26] and a DNA tetrahedron[27] have successfully inhibited oncogenic miRs within cells. in vivo efficacy has also been provided by 3-way junction RNA nanoparticles that efficiently reduce the activity of oncogenic miR-21 and miR-17 in mice,[28,29] by DNA tetrahedron loaded with miR inhibitors for skin anti-aging properties[30] and for miR-22-3p carriers to address a depressive disorder.[31] Additionally, hybrid miR-containing DNA tetrahedron and hydrogel systems have shown in vivo effect in tackling osteonecrosis through combined therapy.[32] While these examples highlight the potential of DNCs for miR-based therapies in cancer, it is noteworthy that their use in treating cardiac diseases remains unexplored.

Here, we present DNCs tailored to address cardiac dysfunction with miR therapies, in particular with application in HF or to mitigate the deleterious effects of cardiac aging. Specifically, our DNCs are designed to modulate the intracellular levels of miR-24-2-5p using an anti-miR approach and consequently, the levels of SERCA2. We have designed and fully characterized two different DNC configurations differing in the position of the miR bait, and thus in the miR capture strategy. Our data demonstrate the proper assembly of both DNC configurations, the specific capture of the target miR and subsequent DNCs disassembly, and their proper stability in biological conditions in vitro, among other features. Interestingly, only one configuration is able to rescue the intracellular levels of SERCA2 in a model cell system. Our anti-miR-24-2-5p DNCs are able to internalize at low levels in human induced pluripotent stem cell-derived cardiomyocytes (iCMs) in vitro, underscoring the opportunity to develop methods to enhance their cell-specific uptake in vivo.

2. Results and Discussion

2.1. Design, Assembly, Structural Characterization, and Nuclease-Mediated Degradation of Anti-miR-Containing DNCs

DNCs were prepared through complementary hybridization of smaller building block units (**Figure 1**) to render nanohydrogel-type nanostructures by adapting previous methods.[33]

Initially, two Y-shaped DNA constructs, Monomer (M) and Stopper (S), each composed by three complementary strands, and one double-stranded DNA serving as linker (L), were assembled in a phosphate saline buffer (PBS) using a thermal gradient. M comprises three dsDNA arms ending in 22-nucleotides (nts) long overhangs fully complementary to the target miR-24-2-5p, thereby acting as anti-miR-24-2-5p. L hybridizes with 12-nts of these overhangs to drive the assembly of the entire DNC. The non-hybridized 10 nts of M act as bait for miR capture. S contains a 12 nts-long overhang in just one arm to block DNC growth. Two types of DNCs were prepared by modifying the position at which L bridges the monomers. Namely, the DNC_A (N_A) was assembled with L hybridizing with the internal part of the M overhang, leaving a 10 nts long external bait. Conversely, DNC_B (N_B) was assembled with L hybridizing with the external part of the M overhang, leaving a 10 nts long internal bait (Figure 1; and Table S1, Supporting Information).

Polyacrylamide gel electrophoresis (PAGE), Dynamic Light Scattering (DLS) and Atomic Force Microscopy (AFM) were employed to assess the proper formation of DNCs. In PAGE (**Figure 2a**), distinct bands for M, S, and L were observed and their mobility, following the order L>S>M, correlated with their respective structural sizes. For N_A and N_B lanes, DNA signals were visibly retained in the wells, smearing toward faster mobility species, indicating correct assembly of small components into larger structures. Agarose gel electrophoresis (AGE) further confirmed correct assembly (Figure S1, Supporting Information), as evidenced by the retarded mobility of DNCs compared to the smaller DNA constructs. DLS data (Figure 2b) and AFM images (Figure 2c) showed increased sizes for the DNCs compared to M.

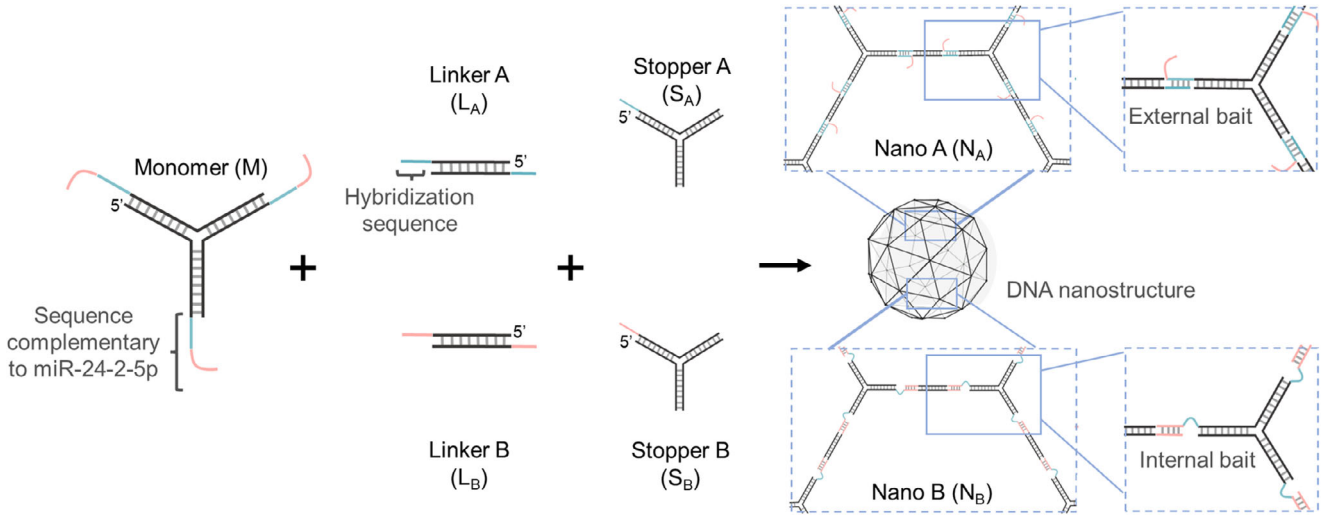

Figure 1. DNCs assembly in their two configurations (N_A and N_B). Complementary sequences between monomer, linker and stopper overhangs are shown in either blue (N_A) or red (N_B). DNCs were assembled by mixing M, S, and L following the ratio 64:1 (M:S) and 1:1.5 (M:L).

Specifically, average hydrodynamic diameters (Dh) of 81 ± 26, 67 ± 15, and 12 ± 2 nm were obtained by DLS for N_A, N_B, and M, respectively, with larger standard deviation observed for N_A (Figure 2b; Figure S2a, Supporting Information). The 10 nts long internal bait present in N_B introduces larger flexibility and hence may facilitate the hybridisation of the linker leading to a narrower size distribution. AFM images taken in dry samples revealed larger averaged sizes for N_A (34 ± 12 nm) and N_B (28 ± 9 nm) compared to M (10 ± 2 nm) (Figure S2b, Supporting Information). The smaller values obtained by AFM compared to DLS

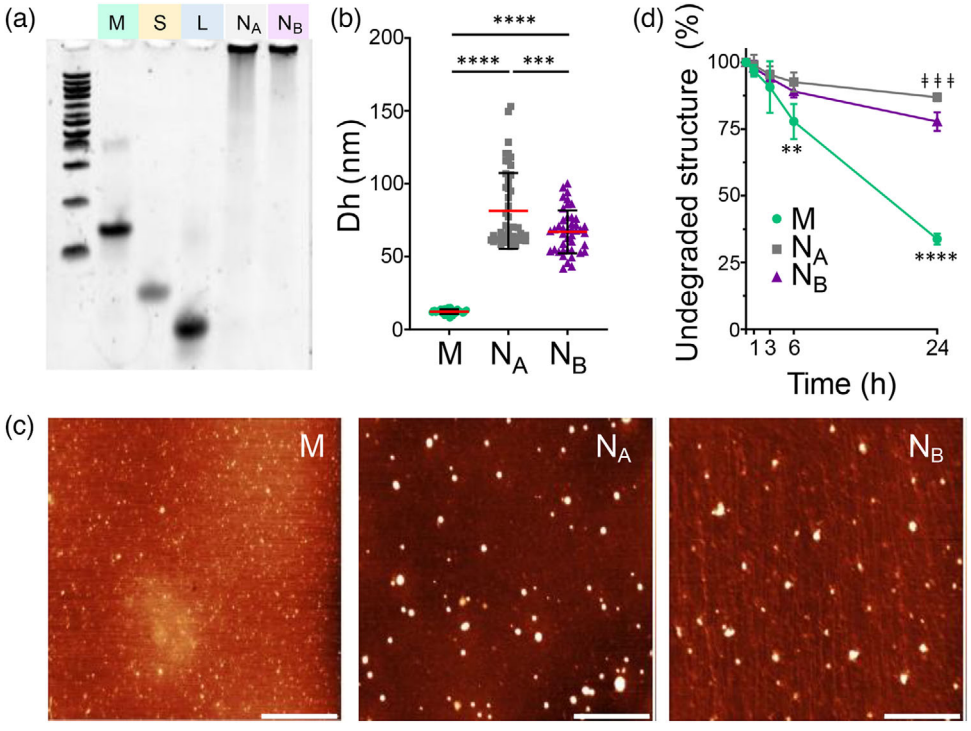

Figure 2. Characterization of the DNCs. a) PAGE showing retarded mobility of the assembled N_A and N_B compared to M, S, and L. 100 bp DNA ladder is included at the most left lane. b) Distribution of the hydrodynamic diameter (Dh) values (in intensity) obtained by DLS of M, N_A, and N_B (individual values and mean ± SD; $n \geq 4$ independent studies of 10 measurement each). c) AFM images (topography) of M, N_A, and N_B. Scale bar is 500 nm; d) Percentage of intact nanostructures incubated in cell culture media with serum over time in hours (h) (mean ± SD; $n = 3$–4; * for comparison of M with both N_A and N_B; ‡ for comparison of N_A with N_B). Significant thresholds were established at: $p \leq 0.05$ (*/‡), $p \leq 0.01$ (**/‡‡), $p \leq 0.001$ (***/‡‡‡), and $p \leq 0.0001$ (****/‡‡‡‡).

may arise from tip compression of the nanostructures, as well as potential compaction of the nanohydrogel-type DNCs in the absence of water.[34–37] DNCs displayed a globular-like morphology in AFM images, which is consistent with the expected structural design for these nanostructures.[33,38,39]

DNCs' biodegradability was studied by evaluating their susceptibility to nuclease-mediated degradation by DNAse I, a major nuclease present in serum.[40] PAGE analysis showed that N_A, N_B, and M are all degraded by DNAse I (Figure S3, Supporting Information), confirming their optimal degradation in biological conditions and supporting their potential as safe, biodegradable nanocarriers.

Next, to assess whether the DNCs maintain their structural integrity under the chemical conditions relevant to subsequent investigations with cultured cells, we analyzed the stability of the DNCs in cell culture media containing 10% of FBS (DMEMc) for different times up to 24 h (h) at 37 °C. A notable degradation of M in DMEMc at 24 h (only 34 ± 2% of intact structure remaining) indicated the vulnerability in serum of the building unit. Instead, N_A and N_B displayed good stability in DMEMc up to 24 h (87 ± 2% and 78 ± 4% of non-degraded structure, respectively), with N_A being significantly more stable than N_B at 24 h (Figure 2d; Figure S4a, Supporting Information). Stability controls were performed by incubating the structures in nuclease-free PBS for 24 h at 37 °C (Figure S4b, Supporting Information), and all structures remained stable, confirming their robustness under nuclease-free physiological conditions. The higher stability of N_A and N_B compared to M in DMEMc, highlights the enhanced protection of the anti-miR sequences by the assembled DNCs in biological media.

Therefore, the designed building units self-assemble into DNA nanohydrogel-type structures bearing anti-miR-24-2-5p sequences with Dh of ≈75 nm. These DNCs are biodegradable but stable in cell culture conditions during 24 h.

2.2. Specific Capture of miR-24-2-5p by DNCs

Prior to the functional assessment in cells, the capability of the assembled DNCs to specifically sequester miR-24-2-5p was evaluated in vitro using PAGE and fluorescence spectroscopy. According to the DNCs design (Figure 1), N_A and N_B are assembled through the hybridization of M with L via 12 complementary nts of M extension over a total of 22 nts. Hence, in the presence of miR 24-2-5p, L is expected to be displaced from M by the miR via toehold-mediated strand displacement, which results into DNCs disassembly. This design of miR-triggered disassembling nanostructures provides an intrinsic structural reporter to confirm successful miR capture. Furthermore, upon recognition of the target miR, the unoccupied anti-miR sequences of inner locations within the DNCs improve their exposure, subsequently potentially increasing the accessibility of the miR to the baits. Finally, this system is expected to facilitate RNase H-mediated degradation of the resulting DNA-RNA heteroduplex in the intracellular media. To probe this disassembly, N_A and N_B were incubated for 1 h at 37 ^{0}C in PBS with the miR-24-2-5p target sequence as either single-stranded DNA (ssDNA) or RNA (ssRNA) (Table S1, Supporting Information). Incubation of M with each target sequence in a molecular ratio anti-miR bait:target strand 1:2 resulted in gel migration retardation of M, supporting effective capture (**Figure 3a**). In the case of N_A and N_B, the non-migrating band of the fully assembled DNCs nearly vanished upon incubation with the target strands at this ratio. Instead, a band corresponding to M with the captured ssDNA or ssRNA was observed, with just a few complexes of smaller size than the original fully assembled DNCs present, which supports successful disassembly of both DNCs (Figure 3a).

The addition of ssRNA at ratio 1:1 (anti-miR bait:target strand) also led to proper disassembly of DNCs, whereas lower molar ratios resulted in only partial disassembly (Figure S5, Supporting Information). The specificity of the interaction was further validated by employing a single-stranded DNA sequence with a random anti-miR sequence with no homology to miR-24-2-5p ($ssDNA_{mock}$) (Table S1, Supporting Information). Neither M nor the DNCs exhibited any interaction with $ssDNA_{mock}$, supporting the selectivity of the bait specifically toward miR-24-2-5p (Figure 3a).

Fluorescence spectroscopy was also employed to quantitatively assess the degree of target sequence capture and its selectivity under physiological temperature (37 °C). To this end, DNCs were designed to hold a Cy3 fluorophore and a BMN-Q535 dark quencher (Figure S6, Supporting Information). Assembled DNCs present quenched Cy3 fluorescence (light down), while disassembly results in unquenching and Cy3 fluorescence emission (light up) (Figure 3b). These fluorescent light down/up DNCs, hereafter referred to as DNC_{LU}, were incubated for 1 h at 37 ^{0}C with the miR-24-2-5p target sequence at 1:2 ratio of anti-miR bait:target strand sequences (Figure 3c,d). Fluorescence intensity was significantly increased for both $DNCs_{LU}$ upon incubation with both ssDNA and ssRNA, whereas no substantial enhancement was observed in the case of the $ssDNA_{mock}$ control (Figure 3c). This result confirmed the specific capability of both $DNCs_{LU}$ to capture the miR-24-2-5p target sequence. The increase in fluorescence signal for N_A in presence of ssRNA was significantly lower than for ssDNA, while fluorescence enhancement for N_B was equally substantial for both ssRNA and ssDNA (Figure 3c,d). This data suggests a more efficient ssRNA-mediated disassembly in the case of N_B than N_A, and hence more efficient capture of the specific miR sequence by N_B than by N_A at physiological temperature. Differences in the stability of the newly formed RNA-DNA heteroduplex could explain this observation. Indeed, melting temperature values from the DNA-DNA duplex fragment between M and L (before displacement) and from DNA-RNA heteroduplex fragment between M and ssRNA (after displacement) are much enhanced in N_B compared to N_A, which may facilitate the disassembly (Figure S7, Supporting Information). Also, steric hindrance may account for this difference,[42] with the external bait (in N_A) producing more steric hindrance for the approach of ssRNA than the internal bait (in N_B).

Overall, both DNCs demonstrated the capacity to specifically capture the miR target sequence in vitro at 37 °C.

2.3. Cell Viability, Intracellularly Stability, and Cell Internalization

Next, we investigated the DNCs bioactivity in vitro. A routine cell line with no expression of miR-24-2-5p, namely HEK293, was chosen as a model system to demonstrate the functionality of the

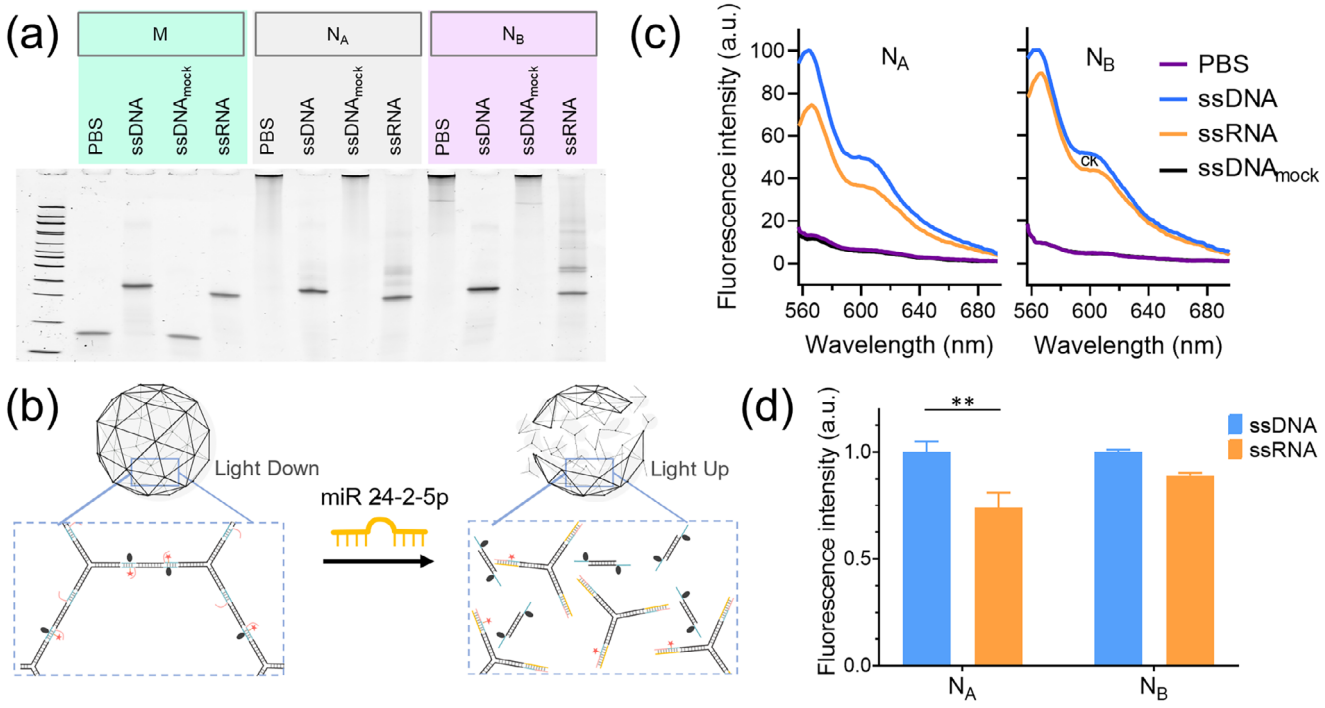

Figure 3. Assessment of capture capacity and specificity of miR-24-2-5p by DNCs. a) PAGE showing interaction of M with the target sequence (as ssDNA, ssRNA) and disassembly of N_A and N_B with the target sequence (as ssDNA and ssRNA) and random sequence ($ssDNA_{mock}$) at ratio 1:2 of anti-miR bait:ssDNA/ssRNA/$ssDNA_{mock}$). 100 bp DNA ladder is included at the most left lane. b) $DNCs_{LU}$ design with fluorescence up detection capacity for disassembly. c) Fluorescence spectra of $DNCs_{LU}$ upon incubation at 37 ^{0}C for 1 h with ssRNA and ssDNA target sequences and $ssDNA_{mock}$ (ratio 1:2 anti-miR bait: target strand). d) Fluorescence fold enhancement of DNCs after incubation with the target ssDNA or ssRNA sequences at a ratio 1:2 anti-miR bait: target strand. Values are normalized by the enhancement observed for ssDNA for each DNC (mean ± SD; $n = 3$). Significance thresholds were established at: $p \leq 0.05$ (*), $p \leq 0.01$ (**).

customized DNCs. Cell proliferation of HEK293 treated with M, N_A, and N_B in DMEMc for up to 24 h paralleled the one of untreated cells (Figure S8, Supporting Information), confirming the lack of cytotoxicity of all the structures.

The internalization capacity in HEK293 of our Cy3-labeled DNCs was evaluated by flow cytometry at different time points for up to 48 h in terms of proportion of loaded cells (**Figure** 4a; Figure S9b, Supporting Information) and loading capacity (Figure 4b). Both Cy3-labeled DNCs, N_A and N_B, were avidly internalized after 7 h of incubation, with more than 50% of $Cy3^+$ cells observed (Figure 4a). They displayed though a low DNC load, as indicated by the nearly unnoticed increase in the Cy3 mean fluorescence intensity (MFI) (Figure 4b). After 24 h of incubation, 100% of the cells had internalized Cy3-labeled DNCs and showed an average

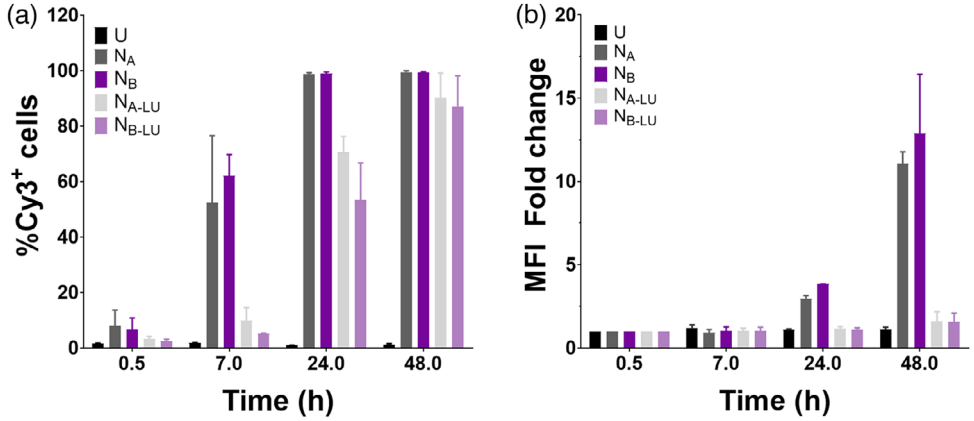

Figure 4. Kinetic of cellular uptake and intracellular stability of anti-miR fragments of DNCs in HEK293 cells. a) Percentage of $Cy3^+$ cells in the presence of Cy3-labeled DNCs or $DNCs_{LU}$ compared to untreated (U) cells reporting uptake or anti-miR trap degradation, respectively. b) Levels of average Cy3 fluorescence per cell (Mean fluorescence, MFI) in the presence of Cy3-labeled DNCs or $DNCs_{LU}$ compared to untreated (U) cells reporting uptake or degradation, respectively (mean ± SD, $n = 2$ with 2–3 technical replicates each).

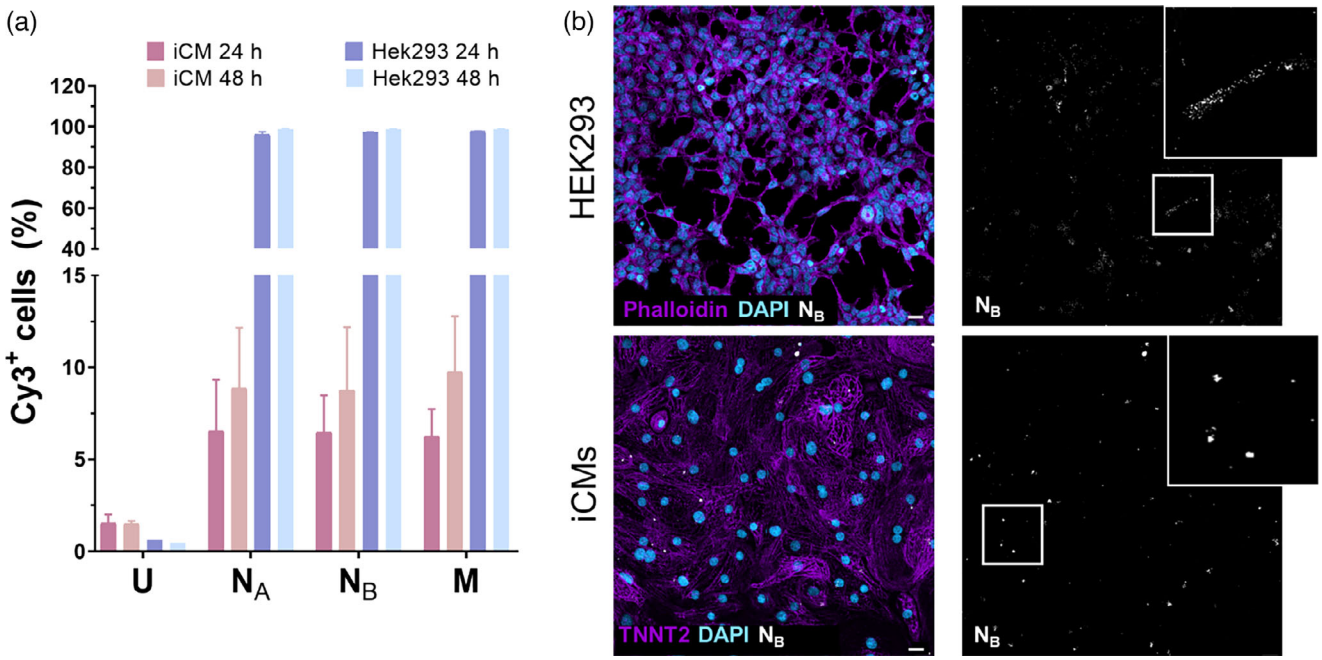

Figure 5. Uptake capacity and subcellular location of DNCs in HEK293 and human iCMs. a) Percentage of $Cy3^+$ cells in both cell types at 24 and 48 h (mean ± SD, n = 2–3 with 1–2 technical replicates each) treated with DNCs or untreated (U). b) Immunostaining with nuclear counterstain (DAPI), Phalloidin (HEK293, top), and TNNT2 (iCMs, bottom) of cells treated with Cy3-labeled N_B. An orthogonal projection is shown. Scale bar corresponds to 20 µm.

of more than three-fold increase in the DNC load per cell compared to the initial time point. Beyond 24 h, the uptake persisted reaching more than ten-fold increase in load. Both N_A and N_B showed comparable internalization capabilities in the HEK293 model cell system.

The intracellular stability of DNCs was tracked using the $DNCs_{LU}$ system (used previously to assess the efficiency of miR capture by DNCs in Figure 3c,d; Figure S6, Supporting Information) and exploiting the lack of expression of miR-24-2-5p in HEK293 cells, which rules out the DNCs disassembly specifically triggered by the miR. In this system, the increase in fluorescence signal can be related to the intracellular degradation of the functional anti-miR fragments of $DNCs_{LU}$. As such, the proportion of cells with intracellular degradation of both $N_{A\text{-}LU}$ and $N_{B\text{-}LU}$ gradually rose over time following the uptake trend and reaching almost 100% of cells harboring degraded DNCs at 48 h (Figure 4a). However, the amount of degraded DNCs per cell of both structures ($N_{A\text{-}LU}$ and $N_{B\text{-}LU}$) remained minimal compared to the initial time point and the total DNC load (Cy3-DNCs) (Figure 4b). No significant differences in the intracellular stability were observed between $N_{A\text{-}LU}$ and $N_{B\text{-}LU}$ (Figure S9, Supporting Information). Altogether, this data indicates high internalization of DNCs maintaining intracellular stability of their functional anti-miR fragment over 48 h in HEK293 cells.

Next, we sought to investigate the internalization capacity of DNCs in the target cell type of interest for the application of the therapy. In contrast to HEK293, but as expected for primary-like hard-to-transfect cells, human iCMs presented significantly lower (around ten-fold less) internalization capacity of the structures (**Figure 5a**). Confocal microscopy confirmed the intracellular location of Cy3-labeled M, N_A and N_B in both HEK293 and iCMs (Figure 5b; Figure S10, Supporting Information). HEK293 presented a more diffuse intracellular pattern of internalized DNCs than iCMs, supporting the observed differences in uptake capacity between cell types.

In summary, the assembled DNCs do not alter cell viability in cultured cells and, upon internalization, they maintain their anti-miR bait sequence stable in the intracellular milieu. However, they show remarkably different internalization capabilities depending on the cell type studied. This highlights the opportunity to implement strategies that enhance the cardiac cell-specific uptake of DNCs to achieve on-target efficacy in vivo.

2.4. DNC Functional Assessment in a Model Cell System

Given the reduced internalization of DNCs in human iCMs, we evaluated the functionality of the developed DNCs in model cell systems via luciferase reporter assay (Figure S11, Supporting Information). Briefly, HEK293 were co-transfected with a luciferase reporter vector containing the *SERCA2* gene sequence (Figure S11a, Supporting Information) and either miR-24-2-5p (Figure S11b, Supporting Information) or a commercial miR mock (miR_{mock}). The miR_{mock} is a control miR that does not interact with human mRNAs, so the luciferase activity in this case represents the basal activity of the model. On the other hand, co-transfection of HEK293 with the reporter vector and miR-24-2-5p indicates the degree of inhibition exerted by the miR on SERCA2 expression (relative to the basal activity of miR_{mock}), as previously reported. [6]

These cellular models were treated with N_A, N_B, M or scramble DNCs (N_{sc}) (**Figure 6**). N_{sc} shares the configuration of N_A and

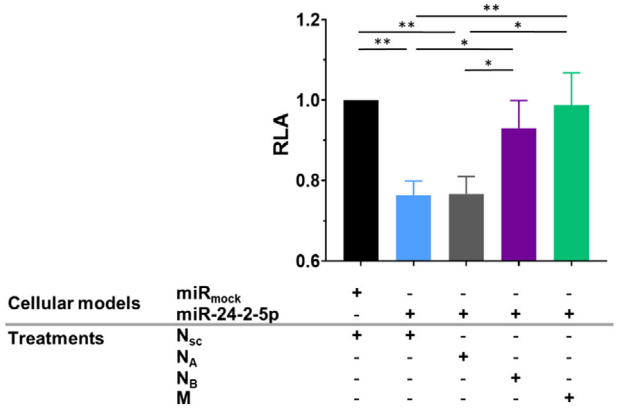

Figure 6. Functional assessment of DNCs in cellular model systems. Relative luciferase activity (RLA) of the *pmiRGLO-SERCA2 vector* reporter vector co-transfected with miR mimics (miR-24-2-5p or miR$_{mock}$) was determined after 24 h treatment with the different DNCs (mean ± SD, $n > 2$ with 3-4 technical replicates in each experiment). Significance thresholds were established at: $p \leq 0.05$ (*) $p \leq 0.01$ (**).

the sequences of M, but with the exception that M$_{sc}$ harbors a random anti-miR sequence that is not complementary to miR-24-2-5p or miR$_{mock}$ (Table S1, Supporting Information). Therefore, N$_{sc}$ is a negative control for the specificity of miR-24-2-5p capture. The combination of the miR$_{mock}$ cells with the N$_{sc}$ treatment gives the basal luciferase activity of the model treated with DNCs. With this set up, miR-24-2-5p transfected cells treated with N$_{sc}$ maintained the described level of miR-24-2-5p-mediated SERCA2 inhibition [6] by 0.76 ± 0.03 fold. When assessing the anti-miR-24-5p treatments, N$_B$ and M specifically and significantly restored the luciferase activity to levels not statistically different to the basal condition, with fold changes of 0.93 ± 0.06 and 0.94 ± 0.06, respectively. Therefore, N$_B$ and M were able to rescue the miR-24-2-5p-mediated inhibition. Instead, N$_A$ did not have an effect, in agreement with the lower capturing capacity of N$_{A\text{-}LU}$ as compared to N$_{B\text{-}LU}$ by fluorometric analysis (Figure 3c,d).

Overall, this result shows higher functional performance of N$_B$ over the N$_A$ in capturing the target miR intracellularly and validates the ability of N$_B$ to regulate the levels of a potentially pathological cardiac miR in vitro using biocompatible DNA nanocarriers.

3. Conclusion

We have successfully developed and characterized biocompatible anti-miR-loaded DNCs that effectively and specifically capture the target miR-24-2-5p in vitro. The DNCs show stability against nuclease degradation in cell culture media up to 24 h and exhibit the capacity to be internalized by HEK293 cells in a biocompatible manner. While DNCs were also internalized in iCMs, the efficiency was significantly lower than in HEK293 cells. Nonetheless, DNCs, particularly N$_B$ and M, exhibit the ability to restore SERCA2 levels in a cellular model system providing proof of concept of efficacy of a new system with therapeutic potential in HF or age-related cardiac dysfunction. Interestingly, the hybridization strategy employed to form DNCs has a discernible impact on their ability to modulate the miR-24-2-5p effect. Namely, the internal miR bait structure N$_B$ functionally outperforms the 3′-end bait N$_A$ structure, highlighting the significance of DNC design in enhancing its performance capabilities. In addition to providing nuclease protection, the larger size exhibited by N$_B$ compared to M, should benefit retarding renal clearance in systemic delivery,[43] making N$_B$ interesting for future in vivo studies.

Our results suggest that DNCs hold promise as carriers for miR therapies targeting human cardiac cells. As a matter of fact, the observed cell-type specific differences emphasize the prospect toward DNCs functionalization to promote efficient and specific carrier uptake by primary cardiac cells in vivo. Strategies to achieve targeted delivery of DNCs to cardiac tissue could exploit the use of heart-specific ligands, such as aptamers[44] or peptides.[45,46] These type of ligands have already demonstrated success in tissue-specific nanoparticle delivery,[47,48] including cardiac targeting.[48] Additionally, the light up system integrated in the reported DNCs, makes them potentially suitable, upon adequate cardiac-targeting engineering, for in vivo preclinical imaging of miR-24-2-5p present in cardiac tissue, and hence interesting for theranostic purposes.

4. Experimental Section

DNCs Design and Assembly: The design of DNCs was conducted based on an adaptation from previous reports.[33] Prior to assembly, all DNA sequences underwent analysis using Nupack[49] and BLAST[50] software. The sequences of all used oligonucleotides can be found in Table S1 (Supporting Information). Unmodified oligos were purchased from IDT (Integrated DNA Technologies, Inc.) and Macrogen, Inc, while labeled oligos were obtained from Biomers.

DNCs were composed by three building units: monomer (M), linker (L), and stopper (S). N$_A$ and N$_B$ share the same M unit, but they differ in L and S. In the case of N$_A$, the 12-nts long extensions of L$_A$ attach via complementary hybridization with the initial 12 nts of the 22-nts long overhangs present in each of the three arms of M. S$_A$ contains only one 12-nts long overhang complementary to the 12-nts long extension of L$_A$. Regarding N$_B$, L$_B$ attaches to the final 12-nts overhang present in each of the three arms of M and to the single 12-nts long overhang in S$_B$.

In Cy3-labeled DNCs, 40% of Cy3 labeled M was added to samples for DNCs assembly. Specifically, 40% of M is labeled with one strand fluorescently functionalized with the Cy3 fluorophore (Table S1, Supporting Information) and 60% of M is added unlabeled. DNCs$_{LU}$ were developed to track ssDNA/ssRNA-mediated disassembly process. To this end, 20% of M$_{LU}$ was Cy3 labeled (present in one of the 3 strands) (Table S1, Supporting Information) and 100% of L$_{LU}$ are labeled with BMNQ535 quenchers (present in the two strands composing L$_{LU}$). Note that M$_{LU}$ contains a single Cy3 label, whereas L$_{LU}$ is labeled with two BMN-Q535 quenchers, one per overhang, to ensure complete fluorescence quenching upon assembly.

M, S, and L were assembled at equimolar oligonucleotide concentration in PBS solution. DNCs were assembled by mixing M, S, and L following the ratio of 64:1 (M:S) and 1:1.5 (M:L). These ratios correspond to molar concentrations of 4 µM of M, 62.5 nM of S and 6.031 µM of L. The assembly of DNA nanostructures (M, S, L, and the DNCs) was carried out in a thermocycler with a thermal-annealing protocol from 95 to 25 °C in 140 steps (0.5 °C per step, 30 s each step). Samples were stored at 4 °C.

Electrophoretic Mobility Shift Assay (EMSA): EMSA was performed using either PAGE or AGE. For PAGE, 20 ng of each DNA sample were loaded. Samples were run for 1 h at 100 V in an 8% polyacrylamide gel immersed in a solution containing 11 mM $MgCl_2$ buffered with 1x Tris-Acetate-EDTA (TAE) (pH = 8.3) (Thermo Fisher, 10 628 403). As a reference, a 100 bp DNA ladder or 1 Kb DNA ladder (New England Biolabs, N3231, and N3232) were run along with the samples. As for AGE, 50 ng of each DNA sample were loaded. Samples were run for 1 h at 100 V in

a 3% agarose gel immersed in an 11 mM $MgCl_2$ 1x TAE running buffer. For subsequent visualization, the gels were stained with GelRed (Biotium, 41 003) and imaged under ultraviolet light transillumination.

Dynamic Light Scattering (DLS): The hydrodynamic sizes of M, N_A, and N_B were measured by DLS. N_A and N_B were folded in PBS at a concentration of 200 ng μL^{-1} and M was folded at a higher concentration of 800 ng μL^{-1} due to its smaller size. Samples were analyzed at 25 °C using the Malvern analytical Zetasizer Nano ZS instrument. The reported values represent the average of ≥4 independent studies of 10 measurement each, consisting of 5 reads per run. Values in intensity were provided.

Atomic Force Microscopy (AFM): For AFM studies, 4 µL of either M, N_A, or N_B at a concentration of 50 ng μL^{-1} were spotted onto freshly exfoliated mica and left to adsorb to the surface for 5 min. Then, sample was washed thrice with filtered Milli-Q water followed by soaking up of excess water using a tissue and slowly drying under a soft air nitrogen steam for 3 min. Samples were analyzed using a Veeco-Bruker Multimode 8 instrument with NGS30 tips (golden silicon probes, force constant 1.2–6.4 N/m, NT-NMD Spectrum Instruments) in tapping mode in air. Images were analyzed using Gwyddion 2.60 Software. The diameters of DNA nanostructures were estimated extracting profiles of individual motifs in the two different axes. The value per particle was the averaged of the profiles of the two different axes. Fifty motifs at least were analyzed to provide the averaged value.

miR Capturing Study: DNCs with the same M concentration (1 µM) were incubated with the ssRNA, ssDNA, or $ssDNA_{mock}$ during 1 h at 37 °C at various molar ratios (bait fragment: anti-miR target sequence). Samples were then analyzed by PAGE as described above. $DNCs_{LU}$ samples were assembled as described for DNCs. For fluorescence spectrophotometry samples were prepared at M concentration (4µM) and diluted 1:5 in PBS (final M concentration of 800 nM) and sequences (ssDNA, ssRNA, $ssDNA_{mock}$) were added to a final concentration of 4.8 µM to match the concentration of bait overhangs for 1:2 ratio of anti-miR bait:target strand sequences. Fluorescence was recorded in a ClarioStar plate reader setting the excitation at 540 nm and the emission window from 556 to 696 nm. Fluorescent measurements were recorded at 37 ^{0}C. Fluorescence curves data were processed with Origin software. Fluorescence maxima was fixed at 565 nm.

DNAse I and Cell Culture Media Mediated DNCs Degradation: Nuclease degradation of M, N_A and N_B was studied through incubation with either DNase I or DMEM supplemented with 10% FBS (DMEMc). Regarding DNase I degradation study, samples were incubated at a DNA concentration of 50 ng μL^{-1} with 4.0, 2.0, 1.0, 0.5, 0.25, 0.125, and 0 U mL^{-1} of DNase I (New England Biolabs, M0303) along with 1x DNase I buffer at 37 °C for 1 h. For the DMEMc degradation study, 50 ng μL^{-1} of M, NA, and NB were incubated with DMEM (Thermo Fisher, 13 476 146) supplemented with 10% FBS (Sigma Aldrich, F7524) at 37 °C during different times: 0, 1, 3, 6, and 24 h. All samples were analyzed using PAGE. The degree of stability was quantified by measuring the decrease in the intensity of the main band corresponding to the non-degraded DNC and the emergence of a smear resulting from degradation compared to time 0 h, using image J. Specifically, the percentage of non-degraded structure was calculated using the following two equations:

$$F = \frac{I}{I + S} \quad (1)$$

$$\%\ \mathrm{NDS} = \frac{F_i}{F_0} \mathrm{x}\ 100 \quad (2)$$

Where F is the fraction of the main band; I, is the intensity of the main band; S, is the intensity of the slurry; % NDS, is the percentage of non-degraded structure; F_i, is the fraction of the main band at every time point and F_0, is the fraction of the main band at the initial time point.

Cell Culture: HEK293 cells were maintained in Minimum Essential Media (MEM) (Biowest, BWSTL0415) supplemented with 10% Fetal Bovine Serum (FBS) (Thermo Fisher, 10 270 106) and 1% Penicillin/Streptomycin (Thermo Fisher, 15 140 122), according to manufacturer's recommendations and passaged regularly when reaching confluence using EDTA 0.5 mM.

The human iPSC line Bj1,[51] kindly provided by Dr Prof. Verfaillie (Katholieke Universiteit Leuven, Belgium), was cultured on vitronectin (Thermo Fisher, A14700) coated dishes with Essential 8 medium (Stem Cell Techonologies, 0 5990) and routinely passaged with EDTA 0.5 mM. iPSC seeded at a density of 100 000 cells cm^{-2} on matrigel (Falcon, 354 277) coated-dishes underwent directed differentiation to cardiomyocytes after 48 h following the Giwi protocol.[52] On day 10, iCMs were enriched and then purified during three days with Cardiomyocyte Purification Medium (CPM), containing RPMI 1640 no glucose (Thermo Fisher, 11 879 020), 2% B27 supplement (Gibco, 17 504 001) and 1% Penicilin/Streptomycin. Finally, iCMs were expanded in cardiomyocyte expansion media (CEM) (RPMI1640 (Biowest, BWSTL0500), 2% B27 Supplement (Thermo Fisher, 17 504 001) supplemented and with 2 µM CHIR99021 (MERCK, SML1046-5MG) following described procedures.[53,54] Before the addition of DNCs, iCMs were incubated with Cardiomyocyte Maintenance Medium (CMM) based on RPMI1640 (Biowest, BWSTL0500) and 2% B27 Supplement (Thermo, 17 504 044).

Cell Viability Assays: HEK293 were seeded in a 96-well plate at a density of 60000 cells cm^{-2} and, after 24 h, M, N_A, and N_B were added at a final concentration of 100 ng μL^{-1} of DNA.

Immediately, three phase contrast images per well were acquired every 2 h during 48 h at 10x magnification in the Incucyte SX5 platform (Sartorius). Image analysis was done in the Incucyte 2021C software by determining the percentage of confluence per well normalized to untreated cells (without DNCs) and normalized to 0 h.

Uptake and Intracellular Stability by Flow Cytometry (FC): The internalization and intracellular stability of DNCs (N_A and N_B) were evaluated in HEK293 cells with 50 ng μL^{-1} of Cy3-labeled DNCs or 50 ng μL^{-1} $DNCs_{LU}$, respectively. HEK293, were seeded in a 96-well plate at a density of 60000 cells cm^{-2}. The day after, DNCs were added and incubated for 0.5, 7, 24, and 48 h before analysis in a Gallios 10Flow Cytometer (Beckman Counter). Uptake capacity was evaluated in HEK293 and iCMs with 100 ng μL^{-1} of Cy3-labeled DNCs after 24 and 48 h of treatment. HEK293 were prepared as for internalization/intracellular stability analysis. iCMs were plated in 48-well plates coated with Geltrex LDEV-Free Reduced Growth Factor Basement Membrane Matrix (Gibco, A1413202), at 60000 cells cm^{-2} and maintained in CEM till nearly confluence. Then, media was replaced by CMM and incubated for another 7 days in CMM to gain maturity before DNCs addition. FC data analysis was performed with FlowJo software. Internalization capacity was determined as the percentage of $Cy3^+$ cells while intracellular stability was calculated as the mean fluorescence intensity (MFI) of each DNCs normalized to the MFI of the initial timepoint (0.5 h).

Immunofluorescence and Imaging: HEK293 and iCMs were prepared as for FC analysis but plated on 10 mm cover slip and incubated with 100 ng μL^{-1} DNCs (N_A, and N_B) and 45 ng μL^{-1} of M for 24 h before fixation with 4% paraformaldehyde. Then, HEK293 were permeabilized with 0,1% saponin and 1% Bovine Serum Albumin (BSA) (Sigma-Aldrich, A9647) in DPBS, stained with 1:100 dilution of Phalloidin Alexa Fluor 488 (Thermo Fisher, A12379) in DPBS for 1 h at room temperature in darkness and finally counterstained with 3 µM DAPI for 20 min (Abcam, ab228549). iCMs were permeabilized and blocked with 0.1%Triton X-100 (CAS 9002-93-1) during 15 min and with undiluted protein block (Agilent, X090930-2) during 25 min, respectively. After DPBS washing, cells were incubated with a 1:100 dilution of primary rabbit antibody anti-human Cardiac Troponin I (Abcam, ab91605) overnight at 4 °C. The secondary antibody, Alexa Fluor 488 goat anti-rabbit IgG (Invitrogen, A11034) diluted 1:1000, was incubated during 30 min in darkness followed by 3 µM DAPI counterstaining as indicated previously.

Images were acquired with a Carl Zeiss LSM 880 Confocal Microscope (Carl Zeiss, Germany) at 40x magnification. Image processing and analysis was performed with ZEN software.

Luciferase Reporter Assays: HEK293 cells were plated in 384-well plates at a density of 100000 cells cm^{-2} and co-transfected with a *SERCA2* luciferase vector[6] (Figure S11, Supporting Information) and miR mimics using Lipofectamine 2000 Transfection Reagent (Invitrogen, 11 668 027)

according to manufacturer's instructions. Specifically, 45 ng of *pmiRGLO-SERCA2* reporter vector (Figure S11a, Supporting Information) and 0.6 pmoles of miR mimic sequences, including hsa-miR-24-2-5p miR Mimic (Cohesion Bioscience, CMH0480) and miR Mimic Negative Control (miR_{mock}) (Cohesion Bioscience, CMH0000) were used. The media was changed after 24 h post-transfection, and, after another 24 h, cells were incubated with 100 ng μl^{-1} of N_A or N_B (45 ng μL^{-1} in the case of M) M for 24 h. Also, 100 ng μl^{-1} of a DNC with a random bait sequence (N_{sc}) was used as negative control (Table S1, Supporting Information). Luciferase reporter assays were conducted using the Dual-Glo Luciferase Assay System (Promega, E2920) following manufacturer's instructions. Luminescence signal produced by the reporter and normalizer proteins, namely Firefly (*Fluc*) and Renilla luciferases, respectively, were measured on the Biotek Synergy HT.

Relative luciferase activity (RLA) was calculated as the ratio of each experimental condition to the basal luciferase activity of the model treated with DNCs, namely the miR_{mock} cellular model treated with N_{sc}. Luminescence values were determined by normalizing the Fluc relative light units (RLUs) to Renilla RLUs in each well.

Statistical Analysis: GraphPad was used for statistical analyses. Data was reported as mean ± standard deviation (SD). One-way ANOVA test was used to compare independent groups. The significance threshold was established at $p \leq 0.05$ (*) and following significance levels were $p \leq 0.01$ (**), $p \leq 0.001$ (***), $p \leq 0.0001$ (****).

Supporting Information

Supporting Information is available from the Wiley Online Library or from the author.

Acknowledgements

Authors acknowledge the following funding: grant LMP128_21 by Gobierno de Aragón, grant PID2020-113003GB-I00 funded by MICIU/AEI/10.13039/501100011033, PID2022-139859OB-I00 funded by MICIU/AEI/10.13039/501100011033 and ERDF, UE and Research Group grants (E47_23R and T39_23R) by Gobierno de Aragón. This study was also supported by MCIN with funding from European Union NextGenerationEU (PRTR-C17.I1). Authors also acknowledge DNABEATS project, Joint Transnational Call 2022 of M-ERA.NET 3, (Horizon 2020 grant agreement No 958174) and supported by grants PCI2023-143390 and PCI2023-143438 funded by MICIU/AEI/10.13039/501100011033 and cofounded by EU. N.H.-B. and M.S.-B. were funded by Gobierno de Aragón fellowships CPB_09_20 and CPB_14_22, respectively. The authors would like to acknowledge the Servicio General de Apoyo a la Investigación-SAI (Universidad de Zaragoza) and Servicios Científico-Técnicos (microscopía, UNATI, y citometría) of CIBA (IISA-IACS-Universidad de Zaragoza) for their support.

Conflict of Interest

The authors declare no conflict of interest.

Author Contributions

The manuscript was written through contributions of all authors. All authors have given approval to the final version of the manuscript.

Data Availability Statement

The data that support the findings of this study are available in ZENODO (10.5281/zenodo.13921161).

Keywords

cardiac dysfunction, DNA nanotechnology, microRNA therapy, toehold-mediated strand displacement

Received: June 4, 2024
Revised: September 8, 2024
Published online: November 1, 2024

[1] World Health Organization (WHO), "Cardiovascular diseases," **2021**.
[2] J. L. Rodgers, J. Jones, S. I. Bolleddu, S. Vanthenapalli, L. E. Rodgers, K. Shah, K. Karia, S. K. Panguluri, *J. Cardiovasc. Dev. Dis.* **2019**, *6*, 19.
[3] M. Zhou, G. Zhao, Y. Zeng, J. Zhu, F. Cheng, W. Liang, *Rev. Cardiovasc. Med.* **2022**, *23*, 135.
[4] R. M. W. Colpaert, M. Calore, *Cells* **2019**, *8*, 737.
[5] R. A. Boon, K. Iekushi, S. Lechner, T. Seeger, A. Fischer, S. Heydt, D. Kaluza, K. Tréguer, G. Carmona, A. Bonauer, A. J. G. Horrevoets, N. Didier, Z. Girmatsion, P. Biliczki, J. R. Ehrlich, H. A. Katus, O. J. Müller, M. Potente, A. M. Zeiher, H. Hermeking, S. Dimmeler, *Nature* **2013**, *495*, 107.
[6] E. Ramos-Marquès, L. García-Mendívil, M. Pérez-Zabalza, H. Santander-Badules, S. Srinivasan, J. C. Oliveros, R. Torres-Pérez, A. Cebollada, J. M. Vallejo-Gil, P. C. Fresneda-Roldán, J. Fañanás-Mastral, M. Vázquez-Sancho, M. Matamala-Adell, J. F. Sorribas-Berjón, J. A. Bellido-Morales, F. J. Mancebón-Sierra, A. S. Vaca-Núñez, C. Ballester-Cuenca, M. Jiménez-Navarro, J. M. Villaescusa, E. Garrido-Huéscar, M. Segovia-Roldán, A. Oliván-Viguera, C. Gómez-González, G. Muñiz, E. Diez, L. Ordovás, E. Pueyo, *Aging Cell* **2021**, *20*, 13383.
[7] K. Gabisonia, G. Prosdocimo, G. D. Aquaro, L. Carlucci, L. Zentilin, I. Secco, H. Ali, L. Braga, N. Gorgodze, F. Bernini, S. Burchielli, C. Collesi, L. Zandonà, G. Sinagra, M. Piacenti, S. Zacchigna, R. Bussani, F. A. Recchia, M. Giacca, *Nature* **2019**, *569*, 418.
[8] R. Hinkel, D. Ramanujam, V. Kaczmarek, A. Howe, K. Klett, C. Beck, A. Dueck, T. Thum, K.-L. Laugwitz, L. Maegdefessel, C. Weber, C. Kupatt, S. Engelhardt, *J. Am. Coll. Cardiol.* **2020**, *75*, 1788.
[9] J. Täubel, W. Hauke, S. Rump, J. Viereck, S. Batkai, J. Poetzsch, L. Rode, H. Weigt, C. Genschel, U. Lorch, C. Theek, A. A. Levin, J. Bauersachs, S. D. Solomon, T. Thum, *Eur. Heart J.* **2021**, *42*, 178.
[10] E. Van Rooij, L. B. Sutherland, N. Liu, A. H. Williams, J. McAnally, R. D. Gerard, J. A. Richardson, E. N. Olson, *Proc. Natl. Acad. Sci. USA* **2006**, *103*, 18255.
[11] J. Wang, W. Huang, R. Xu, Y. Nie, X. Cao, J. Meng, X. Xu, S. Hu, Z. Zheng, *J. Cell. Mol. Med.* **2012**, *16*, 2150.
[12] T. Ma, F. Qiu, Y. Gong, H. Cao, G. Dai, D. Sun, D. Zhu, H. Lei, Z. Liu, L. Gao, *Theranostics* **2023**, *13*, 3826.
[13] L. Zhihao, N. Jingyu, L. Lan, S. Michael, G. Rui, B. Xiyun, L. Xiaozhi, F. Guanwei, *Heart Failure Rev.* **2020**, *25*, 523.
[14] B. Greenberg, J. Butler, G. M. Felker, P. Ponikowski, A. A. Voors, J. M. Pogoda, R. Provost, J. Guerrero, R. J. Hajjar, K. M. Zsebo, *Gene Ther.* **2016**, *23*, 313.
[15] C. Diener, A. Keller, E. Meese, *Trends Genet.* **2022**, *38*, 613.
[16] M. Cassani, S. Fernandes, J. Vrbsky, E. Ergir, F. Cavalieri, G. Forte, *Front. Bioeng. Biotechnol.* **2020**, *8*, 506432.
[17] C. R. Lucas, P. D. Halley, A. A. Chowdury, B. K. Harrington, L. Beaver, R. Lapalombella, A. J. Johnson, E. K. Hertlein, M. A. Phelps, J. C. Byrd, C. E. Castro, *Small* **2022**, *18*, 2108063.
[18] B. R. Madhanagopal, S. Zhang, E. Demirel, H. Wady, A. R. Chandrasekaran, *Trends Biochem. Sci.* **2018**, *43*, 997.
[19] L. Zhu, J. Luo, K. Ren, *J. Mater. Chem. B* **2023**, *11*, 261.

[20] J. Huang, W. Ma, H. Sun, H. Wang, X. He, H. Cheng, M. Huang, Y. Lei, K. Wang, *ACS Appl. Bio Mater.* **2020**, *3*, 2779.
[21] Q. Chi, Z. Yang, K. Xu, C. Wang, H. Liang, *Front. Pharmacol.* **2020**, *10*, 1585.
[22] S. Raniolo, V. Unida, G. Vindigni, C. Stolfi, F. Iacovelli, A. Desideri, S. Biocca, *Cell Death Dis.* **2021**, *12*, 7.
[23] K. Zhang, J. Liu, Q. Song, X. Yang, D. Wang, W. Liu, J. Shi, Z. Zhang, *ACS Appl. Mater. Interfaces* **2019**, *11*, 46604.
[24] S. Nahar, A. K. Nayak, A. Ghosh, U. Subudhi, S. Maiti, *Nanoscale* **2017**, *10*, 195.
[25] K. Kumari, A. Kar, A. K. Nayak, S. K. Mishra, U. Subudhi, *RSC Adv.* **2021**, *11*, 10670.
[26] A. Kar, K. Kumari, S. K. Mishra, U. Subudhi, *BMC Cancer* **2022**, *22*, 1332.
[27] L. Yu, S. Yang, Z. Liu, X. Qiu, X. Tang, S. Zhao, H. Xu, M. Gao, J. Bao, L. Zhang, D. Luo, K. Chang, M. Chen, *Mater. Today Bio* **2022**, *15*, 100276.
[28] D. Shu, H. Li, Y. Shu, G. Xiong, W. E. Carson, F. Haque, R. Xu, P. Guo, *ACS Nano* **2015**, *9*, 9731.
[29] D. W. Binzel, Y. Shu, H. Li, M. Sun, Q. Zhang, D. Shu, B. Guo, P. Guo, *Mol. Ther.* **2016**, *24*, 1267.
[30] S. Li, Y. Liu, T. Zhang, S. Lin, S. Shi, J. He, Y. Xie, X. Cai, T. Tian, Y. Lin, *Adv. Mater.* **2022**, *34*, 2204287.
[31] Y. Luo, X. Yang, Y. Du, Y. Dou, W. Cui, J. Li, J. Wei, X. Ma, Y. Lin, *ACS Appl. Mater. Interfaces* **2023**, *15*, 29813.
[32] D. Li, Z. Yang, Y. Luo, X. Zhao, M. Tian, P. Kang, *Adv. Healthcare Mater.* **2022**, *11*, 2101412.
[33] J. Li, C. Zheng, S. Cansiz, C. Wu, J. Xu, C. Cui, Y. Liu, W. Hou, Y. Wang, L. Zhang, I.-T. Teng, H.-H. Yang, W. Tan, *J. Am. Chem. Soc.* **2015**, *137*, 1412.
[34] P. J. Kolbeck, M. Dass, I. V. Martynenko, R. J. A. van Dijk-Moes, K. J. H. Brouwer, A. van Blaaderen, W. Vanderlinden, T. Liedl, J. Lipfert, *Nano Lett.* **2023**, *23*, 1236.
[35] W. Song, P. Song, Y. Sun, Z. Zhang, H. Zhou, X. Zhang, P. He, *ACS Biomater. Sci. Eng.* **2021**, *7*, 5165.
[36] L. Eswaran, G. Kazimirsky, G. Byk, *Pharm.* **2023**, *15*, 332.
[37] H. Zhu, J. Wu, J. Zhao, L.e Yu, B. R. Liyarita, X. Xu, Y. Xiao, X. Hu, S. Shao, J. Liu, X. Wang, F. Shao, *Acta Biomater.* **2024**, *175*, 240.
[38] Y. Hu, S. Gao, H. Lu, S. Tan, F. Chen, Y. Ke, J. Y. Ying, *Nano Lett.* **2023**, *23*, 9778.
[39] C. Xu, Q. Liu, J. Shi, Z. Liu, Z. Lei, C. Dai, W. Shi, X. Xu, Y. Guo, *ACS Appl. Nano Mater.* **2024**, *7*, 19143.
[40] L. Lauková, B. Konečná, Ľ. Janovičová, B. Vlková, P. Celec, *Biomolecules* **2020**, *10*, 1036.
[41] H. Auvinen, H. Zhang, Nonappa, A. K., E. H. Niemelä, S. Nummelin, A. Correia, H. A. Santos, V. Linko, M. A. Kostiainen, *Adv. Healthcare Mater.* **2017**, *6*, 1700692.
[42] D. Lysne, T. Hachigian, C. Thachuk, J. Lee, E. Graugnard, *J. Am. Chem. Soc.* **2023**, *145*, 16691.
[43] J. Di, X. Gao, Y. Du, H. Zhang, J. Gao, A. Zheng, *Asian J. Pharm. Sci.* **2021**, *16*, 444.
[44] S. Philippou, N. P. Mastroyiannopoulos, M. Tomazou, A. Oulas, M. Ackers-Johnson, R. S. Foo, G. M. Spyrou, L. A. Phylactou, *Pharmaceuticals (Basel)* **2023**, *16*, 1264.
[45] M. J. McGuire, K. N. Samli, S. A. Johnston, K. C. Brown, *J. Mol. Biol.* **2004**, *342*, 171.
[46] S. Rana, K. Datta, T. L. Reddy, E. Chatterjee, P. Sen, M. Pal-Bhadra, U. Bhadra, A. Pramanik, P. Pramanik, M. Chawla-Sarkar, S. Sarkar, *J. Controlled Release* **2015**, *200*, 167.
[47] C. Liang, B. Guo, H. Wu, N. Shao, D. Li, J. Liu, L. Dang, C. Wang, H. Li, S. Li, W. K. Lau, Y. Cao, Z. Yang, C. Lu, X. He, D. W. T. Au, X. Pan, B.-T. Zhang, C. Lu, H. Zhang, K. Yue, A. Qian, P. Shang, J. Xu, L. Xiao, Z. Bian, W. Tan, Z. Liang, F. He, L. Zhang, et al., *Nat. Med.* **2015**, *21*, 288.
[48] X. Zhao, W. Luo, J. Hu, L. Zuo, J. Wang, R. Hu, B. O. Wang, L. Xu, J. Li, M. Wu, P. Li, L. Liu, *J. Nanobiotechnol.* **2018**, *16*, 36.
[49] J. N. Zadeh, C. D. Steenberg, J. S. Bois, B. R. Wolfe, M. B. Pierce, A. R. Khan, R. M. Dirks, N. A. Pierce, *J. Comput. Chem.* **2011**, *32*, 170.
[50] S. F. Altschul, W. Gish, W. Miller, E. W. Myers, D. J. Lipman, *J. Mol. Biol.* **1990**, *215*, 403.
[51] L. Ordovás, R. Boon, M. Pistoni, Y. Chen, E. Wolfs, W. Guo, R. Sambathkumar, S. Bobis-Wozowicz, N. Helsen, J. Vanhove, P. Berckmans, Q. Cai, K. Vanuytsel, K. Eggermont, V. Vanslembrouck, B. Z. Schmidt, S. Raitano, L. Van Den Bosch, Y. Nahmias, T. Cathomen, T. Struys, C. M. Verfaillie, *Stem Cell Rep.* **2015**, *5*, 918.
[52] X. Lian, C. Hsiao, G. Wilson, K. Zhu, L. B. Hazeltine, S. M. Azarin, K. K. Raval, J. Zhang, T. J. Kamp, S. P. Palecek, *Proc. Natl. Acad. Sci. USA* **2012**, *109*, E1848.
[53] J. W. Buikema, S. Lee, W. R. Goodyer, R. G. Maas, O. Chirikian, G. Li, Y. Miao, S. L. Paige, D. Lee, H. Wu, D. T. Paik, S. Rhee, L. Tian, F. X. Galdos, N. Puluca, B. Beyersdorf, J. Hu, A. Beck, S. Venkamatran, S. Swami, P. Wijnker, M. Schuldt, L. M. Dorsch, A. van Mil, K. Red-Horse, J. Y. Wu, C. Geisen, M. Hesse, V. Serpooshan, S. Jovinge, et al., *Cell Stem Cell* **2020**, *27*, 50.
[54] R. G. C. Maas, S. Lee, M. Harakalova, C. J. B. Snijders Blok, W. R. Goodyer, J. Hjortnaes, P. A. F. M. Doevendans, L. W. Van Laake, J. van der Velden, F. W. Asselbergs, J. C. Wu, J. P. G. Sluijter, S. M. Wu, J. W. Buikema, *STAR Protoc.* **2021**, *2*, 100334.